Research Article Vol. 5, No. 10 / October 2018 / Optica 1304

Kerr-microresonator solitons from a chirped background

Daniel C. Cole,[1,2,*] Jordan R. Stone,[1,2] Miro Erkintalo,[3] Ki Youl Yang,[4] Xu Yi,[4] Kerry J. Vahala,[4] and Scott B. Papp[1,2]

[1]National Institute of Standards and Technology (NIST), Boulder, Colorado 80305, USA
[2]Department of Physics, University of Colorado, Boulder, Colorado 80309, USA
[3]Dodd-Walls Centre for Photonic and Quantum Technologies, Department of Physics, University of Auckland, Auckland 1142, New Zealand
[4]T. J. Watson Laboratory of Applied Physics, California Institute of Technology, Pasadena, California 91125, USA
*Corresponding author: daniel.cole@nist.gov

Received 5 July 2018; revised 18 September 2018; accepted 20 September 2018 (Doc. ID 337882); published 16 October 2018

Optical frequency combs based on solitons in nonlinear microresonators open up new regimes for optical metrology and signal processing across a range of expanding and emerging applications. In this work, we advance these combs toward applications by demonstrating protected single-soliton formation and operation in a Kerr-nonlinear microresonator using a phase-modulated pump laser. Phase modulation gives rise to spatially/temporally varying effective loss and detuning parameters, leading to an operation regime in which multi-soliton degeneracy is lifted and a single soliton is the only observable behavior. We achieve direct, on-demand excitation of single solitons as indicated by reversal of the characteristic "soliton step." Phase modulation also enables precise, high bandwidth control of the soliton pulse train's properties, and we measure dynamics that agree closely with simulations. We show that the technique can be extended to high-repetition-frequency Kerr solitons through subharmonic phase modulation. These results will facilitate straightforward generation and control of Kerr-soliton microcombs for integrated photonics systems.

OCIS codes: (190.5530) Pulse propagation and temporal solitons; (140.3948) Microcavity devices.

https://doi.org/10.1364/OPTICA.5.001304

1. INTRODUCTION

Dissipative temporal cavity solitons in Kerr microresonators [1–4] have the potential to provide the revolutionary capabilities of frequency combs in a chip-integrable platform. This would extend the reach of frequency combs to applications in communications, computation, and sensing with low size, weight, and power. Progress has come rapidly in the field of microresonator-soliton-based frequency combs, but for these combs to reach applications, simple, repeatable, and platform-independent methods of soliton generation and control are needed. The basic challenge is that solitons in microresonators are independent excitations, and a resonator can host zero, one, or many co-circulating solitons at a given pump-laser power and frequency. Further, under normal conditions these solitons can be generated only by condensation from extended modulation-instability (MI) patterns (primary comb/Turing patterns, or noisy comb/spatiotemporal chaos) that provide appropriate initial perturbations. Thermal stability must be maintained as the intracavity power drops during the transition from a high-duty-cycle MI pattern to a low-duty-cycle soliton. A variety of schemes have been demonstrated to address these challenges and obtain single solitons [5–9], and many achieve excellent performance. However, in general these schemes increase procedural complexity by exploiting nonadiabatic variations in pump-laser power and frequency, and/or involve at least some amount of stochastic fluctuation in the output.

One notable possibility is modulation of the pump laser at a frequency near the resonator free-spectral range (FSR) [10–13], which can enable deterministic condensation of either one or zero solitons from an MI pattern. Further, it has been demonstrated that phase modulation (PM) can facilitate generation and control of single solitons [12,14,15]. In this article we theoretically describe and then experimentally demonstrate the use of a phase-modulated pump laser for deterministic excitation of single solitons directly from a chirped background that remains otherwise stable, as was proposed in Ref. [16]; the result is a train of solitons spaced by the round-trip time exiting the resonator, as shown in Fig. 1(a). Importantly, this scheme requires no transient perturbation to the system parameters for soliton generation. In addition to exploring soliton generation, we also demonstrate that PM at the FSR can be used for microsecond-level control of the pulse train's repetition rate, and we conclude by discussing how the technique can be applied to resonators with FSR too high to be directly electronically accessible.

2. PHYSICAL MECHANISM AND THEORETICAL EXPLORATION OF THE CONCEPT

Our results demonstrate a regime in which single-soliton operation is fundamentally protected without the degeneracy between $N = 0, 1$ and many solitons that exists for a continuous-wave (CW) pump laser. To motivate the experimental work that

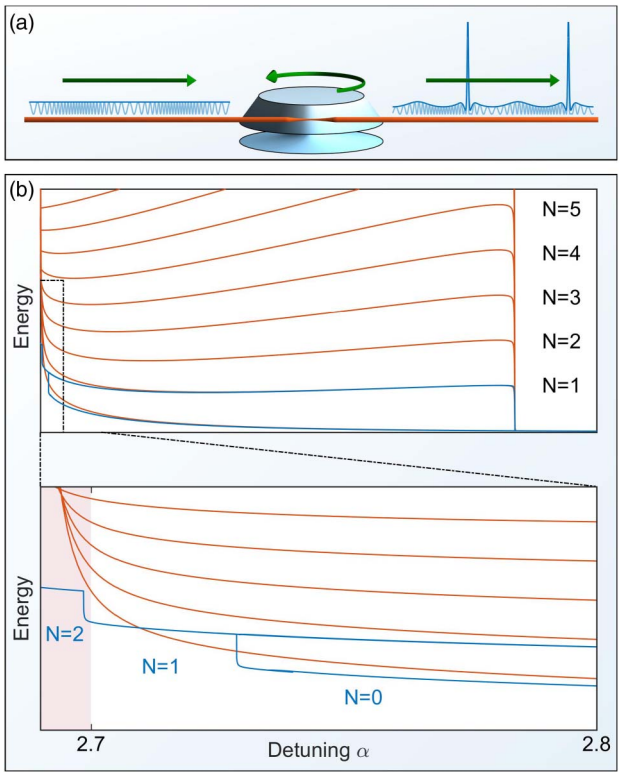

Fig. 1. (a) Schematic for soliton generation in a PM-pumped resonator, neglecting interference at the output. (b) Simulated energy-level diagrams for the CW- (orange) and PM-pumped (blue, $\delta_{PM} = \pi$) resonator for $F^2 = 4$, $\beta_2 = -0.0187$. With PM, an interval in α exists for which the single soliton is the only available energy level. This interval is fairly narrow, but we find that it is readily accessible in experiment. We also observe non-stationary states for values of $\alpha \leq 2.7$ in the PM case (red shading); whether the system exhibits one of these non-stationary states or an $N = 2$ soliton state is determined by the initial conditions that seed the formation of the soliton ensemble.

follows, we begin by presenting theoretical results that illustrate the utility of a PM pump. We use the nonlinear partial-differential Lugiato–Lefever equation (LLE) with modification of the driving term for phase modulation with depth δ_{PM} [1,16–19]:

$$\frac{\partial \psi}{\partial \tau} = -(1 + i\alpha)\psi + i|\psi|^2\psi - i\frac{\beta_2}{2}\frac{\partial^2 \psi}{\partial \theta^2} + Fe^{i\delta_{PM}\cos\theta}. \quad (1)$$

The normalized quantities used in the LLE are defined as follows [17]: ψ is the envelope for the intracavity field normalized so that $|\psi|^2 = 1$ at the absolute threshold for parametric oscillation; $\tau = t/2\tau_{ph}$, where t is the time and $\tau_{ph} = 1/2\pi\Delta\nu$ is the cavity photon lifetime, where $\Delta\nu$ is the cavity resonance linewidth; $\alpha = 2(\nu_0 - \nu_{pump})/\Delta\nu$ is the detuning between the pumped resonance with frequency ν_0 and the pump laser with frequency ν_{pump}; F is the pump strength normalized so that $F^2 = 1$ at the absolute threshold for parametric oscillation; and $\beta_2 = -2D_2/2\pi\Delta\nu < 0$ is the anomalous resonator dispersion, with $D_2/2\pi = \partial^2\nu_\mu/\partial\mu^2|_{\mu=0} > 0$, where ν_μ represents the set of cavity resonance frequencies and $\mu = 0$ indexes the pumped mode. The azimuthal angle θ co-rotates at the frequency f_{PM}, which is presently assumed to be equal to the FSR. We emphasize for clarity that throughout this paper $\alpha > 0$, and, therefore, that the pump laser is always "red detuned" from the cavity resonance; decreasing (increasing) α corresponds to increasing (decreasing) the laser frequency ν_{pump} and moving it closer to (further from) the linear cavity resonance.

We perform simulations of the LLE to investigate soliton degeneracy for the range of pump-laser detunings over which solitons exist. We use a fourth-order Runge–Kutta algorithm in the interaction picture [20] with adaptive step size [21]. The resulting soliton-energy-level diagrams for the CW case ($\delta_{PM} = 0$) and the PM case ($\delta_{PM} = \pi$) are shown in Fig. 1(b). We find that PM transforms the resonator excitation spectrum from a series of $N = 0, 1, 2, \ldots, N_{max}$ solitons to a smaller number of available energy levels. In particular, for detuning α slightly greater than the lower bound for soliton existence (below which lie extended MI patterns), a single level $N = 1$ is the only available state, and soliton degeneracy is eliminated.

The elimination of degeneracy and emergence of the protected $N = 1$ level occurs as a result of spatial/temporal variations of effective loss and detuning parameters that result from the phase modulation. We can obtain an approximation for these parameters by inserting the ansatz $\psi(\theta, \tau) = \varphi(\theta, \tau)e^{i\delta_{PM}\cos\theta}$ into Eq. (1) [15]. By expanding the second-derivative term and setting derivatives of φ to zero we arrive at an equation for the quasi-CW background in the PM-pumped resonator:

$$F = (\gamma(\theta) + i\alpha_{eff}(\theta))\varphi - i|\varphi|^2\varphi. \quad (2)$$

The effective loss and detuning terms are

$$\gamma(\theta) = 1 + \frac{\beta_2}{2}\delta_{PM}\cos\theta, \quad (3)$$

$$\alpha_{eff}(\theta) = \alpha - \frac{\beta_2}{2}\delta_{PM}^2\sin^2\theta. \quad (4)$$

The field ψ can be approximated using these local parameters:

$$\psi = \frac{Fe^{i\delta_{PM}\cos\theta}}{\gamma(\theta) + i(\alpha_{eff}(\theta) - \rho(\theta))}, \quad (5)$$

where $\rho(\theta) = |\varphi(\theta)|^2$ is the (smallest real) solution to the cubic polynomial in ρ obtained by taking the modulus-square of Eq. (2):

$$F^2 = (\gamma(\theta)^2 + (\alpha_{eff}(\theta) - \rho(\theta))^2)\rho(\theta). \quad (6)$$

In neglecting the spatial derivatives of φ but retaining the derivatives of the term $e^{i\delta_{PM}\cos\theta}$, we make the approximation that the dominant effect of dispersion is its action on the existing phase-modulation spectrum. We note that a full analysis of the rich behavior of Eq. (1) without this approximation remains a promising avenue for future research.

Figure 2(a) compares the predictions of simulations of the LLE (color) and the analytical model discussed immediately above (black) for the quasi-CW background in the resonator in the presence of phase modulation. The two agree quantitatively for weak modulation ($\delta_{PM} = \frac{\pi}{2}$, blue) and qualitatively for larger depth ($\delta_{PM} = 4\pi$, green); both indicate that the field ψ exhibits amplitude variations due to spatially varying effective loss and detuning. These parameters determine whether the quasi-CW background locally (as a function of θ) exhibits the bistability that is well known in the case of a CW pump laser [19,22], which suggests a mechanism for spontaneous single-soliton generation: as α is decreased, the stable effectively red-detuned branch of the resonance locally vanishes at the larger peak of the quasi-CW

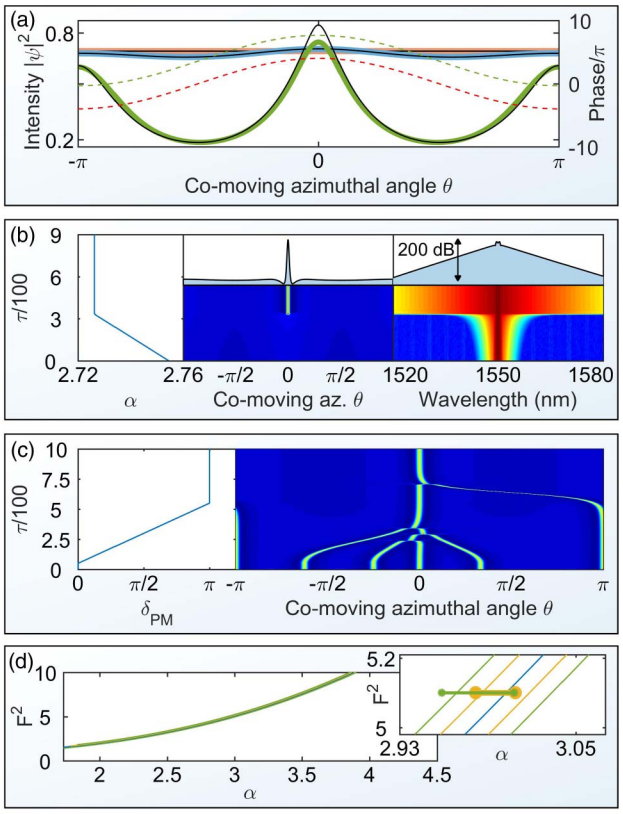

Fig. 2. (a) Simulated quasi-CW background intensity without (orange) and with PM of depth $\pi/2$ (blue) and 4π (green), with $F^2 = 3$ and $\beta_2 = -0.02$, with analytical approximations in black. Here α is slightly larger than α_1, the critical value for soliton formation. Dashed traces show the simulated phase profile of the field ψ (green) and of the driving term $Fe^{i\delta_{PM}\cos\theta}$ (red) with modulation depth 4π. The phase of the field is very nearly the phase of the drive plus a constant offset. (b) A simulation of spontaneous single-soliton generation using a phase-modulated pump laser with $\delta_{PM} = \pi$, $F^2 = 4$, and $\beta = -0.0187$. Left: α is decreased smoothly as a function of time τ and then held constant after a soliton is generated. Middle: false-color plot of the intensity in the cavity as a function of time, with the final intensity shown above. Right: false-color plot of the comb spectrum on a logarithmic scale as a function of time, assuming a repetition rate of 22 GHz. Final spectrum is shown above. (c) A simulation of the collapse of a soliton ensemble to $N = 1$ with initial $N = 5$ for $\alpha = 2.8$, $F^2 = 4$, and $\beta = -0.0187$. To slow down the initial dynamics for clarity, the modulation depth is initialized at $\delta_{PM} = 0$, and then linearly ramped to $\delta_{PM} = \pi$ from $\tau = 50$ to $\tau = 550$. We note that the simulations presented in parts (b) and (c) are similar to simulations presented in Ref. [16]; we present these for clarity without claiming novelty. (d) Plots of approximations (obtained as described in the text, $\beta_2 = -0.0187$) to the values α_1 and α_2 of detuning at which the first soliton and a second soliton are generated, respectively, with a zoomed plot depicting details in the upper right. Several values of PM depth are plotted: $\delta_{PM} = 0$ (blue), $\delta_{PM} = \pi$ (yellow), and $\delta_{PM} = 2\pi$ (green). For each the line to the right is α_1 and the line to the left is α_2; the single line for $\delta_{PM} = 0$ represents the line at which the bistability of the CW background vanishes everywhere in this case. Horizontal lines indicate the interval $\alpha_2 < \alpha < \alpha_1$ obtained in the corresponding LLE simulations with $F^2 = 5.1$.

background at $\theta = 0$, leading to the formation of a soliton. If α is decreased further, the stable effectively red-detuned branch vanishes at the smaller peak at $\theta = \pi$ and a second soliton is formed. By following the analysis in, e.g., Ref. [19] [Eqs. (11)–(14)], we can approximate the detunings α_1 and α_2 where the first and second solitons are generated, respectively, by determining at what detuning the red-detuned branch vanishes for $\theta = 0$ and $\theta = \pi$. For parameters matching the level diagram shown in Fig. 1(b), this predicts generation of the first soliton at $\alpha_1 = 2.741$ and generation of the second at $\alpha_2 = 2.705$, in excellent agreement with the values $\alpha_1 = 2.729$ and $\alpha_2 = 2.699$ obtained in numerical simulations. A simulation of single-soliton generation enabled by pump phase modulation is shown in Fig. 2(b).

If solitons exist at $\theta \neq 0$ in a PM-pumped cavity, they drift to the intracavity intensity maximum at $\theta = 0$ [15], making superpositions of $N > 1$ solitons unstable and practically forbidden for values of detuning $\alpha > \alpha_2$ (for $\alpha \leq \alpha_2$, a second soliton is spontaneously generated at $\theta = \pi$ and persists there). We depict the simulated collapse to $N = 1$ of such a superposition in Fig. 2(c). Thus, over the range of detuning $\alpha_2 < \alpha < \alpha_1$, application of PM to the pump laser removes the degeneracy between $N = 1$ and $N = 0$ and also between $N = 1$ and $N > 1$ solitons. Single-soliton generation and operation then simply require tuning the pump power and frequency to appropriate values, regardless of initial conditions.

Quantitative determination of the full soliton level structure plotted in Fig. 1(b) is numerically quite involved. However, a qualitative estimate of the dependence of the detuning interval $\alpha_2 < \alpha < \alpha_1$ for protected single-soliton generation and operation on pump power F^2 and modulation depth δ_{PM} can be obtained by generalizing the process described above: as a function of F^2 and δ_{PM}, one determines at what values of detuning the bistability vanishes for $\theta = 0$ (defining α_1) and $\theta = \pi$ (defining α_2). We present example approximations in Fig. 2(d). The basic observation is that the interval between α_1 and α_2 over which single-soliton operation is protected increases in size as δ_{PM} increases, as a result of the scaling of the θ-dependence of $\gamma(\theta)$ with δ_{PM} in Eq. (3). In a sample comparison of these approximations with a determination of α_1 and α_2 in an LLE simulation we find that this basic observation holds, but that the prediction for the absolute location of the interval $\alpha_2 < \alpha < \alpha_1$ becomes less accurate for larger δ_{PM}; this is consistent with the greater deviation between approximation and simulation at higher δ_{PM} seen in Fig. 2(a).

Before discussing our experimental implementation of the approach described above, we note that it is natural to consider whether a similar technique can be employed using *amplitude* modulation (AM) outside of the pulsed-pumping limit [13] (this limit requires prior generation of a train of temporally short input pulses, which brings additional complexity). While we have not conducted an exhaustive study of soliton generation with AM, as that is not the primary subject of this work, our preliminary simulations show that AM can indeed be used to spontaneously generate single solitons. Specifically, simulations indicate that one implementation with complexity comparable to our PM technique, in which a single Mach–Zehnder-type modulator with sinusoidal modulation is used to generate a 50% duty-cycle train of nearly flat-topped pulses (see Ref. [23]), is likely to be successful under a somewhat smaller range of parameters than the PM scheme we discuss here. A full quantitative study of AM is, however, beyond the scope of the present work, and is accordingly left as a promising avenue for future research.

3. EXPERIMENTAL RESULTS: SOLITON GENERATION

We implement the approach described above to realize deterministic generation of single solitons without condensation from an extended pattern. Our approach is summarized in Fig. 3, and results are depicted in Fig. 4. We use a 22 GHz FSR silica wedge resonator with $\Delta\nu \sim 1.5$ MHz linewidth [24] (loaded $Q \sim 129$ million, see also Ref. [25]), pumped by a laser with normalized power F^2 between 2 and 6, phase modulated at a rate $f_{\mathrm{PM}} \sim 22$ GHz with relatively small depth $\delta_{\mathrm{PM}} \sim \pi$. The pump laser is derived from a seed CW laser using a single-sideband modulator driven by a voltage-controlled oscillator (VCO) [25], yielding high frequency-control bandwidth. To overcome the challenges presented by thermal instabilities [26], we also address the resonance with a counter-propagating probe beam that is frequency shifted in an acousto-optic modulator (AOM) by $f_{\mathrm{AOM}} = 55$ MHz. We phase modulate this probe beam at a variable frequency $f_{\mathrm{PDH}} < 55$ MHz to enable Pound–Drever–Hall (PDH) locking of the red-detuned PDH sideband of the probe beam to the resonance [25]; the lock is achieved by feeding back to the pump-laser frequency using the VCO. This enables real-time measurement and control of the detuning $\nu_0 - \nu_{\mathrm{pump}}$ according to $\nu_0 - \nu_{\mathrm{pump}} = f_{\mathrm{AOM}} - f_{\mathrm{PDH}}$. A frequency-domain depiction of our detuning-control system is presented in Fig. 3(a), and a schematic depiction of the components used to realize this scheme is shown in Fig. 3(b). Future work could simplify the apparatus while maintaining useful detuning stabilization and control.

To generate solitons we decrease the detuning from a large initial value (~40 MHz) by increasing the frequency f_{PDH} of the PDH modulation—this is done by simply turning the frequency knob on the function generator by hand. A soliton is generated when the detuning is near 5 MHz (dependent upon the pump power and coupling condition). Measuring the power converted through four-wave mixing to new frequencies, the "comb power," reveals a step upon soliton formation, shown in Fig. 4(a). This indicates direct generation of a soliton from the background, and represents a reversal of the characteristic "soliton step" that typically signals condensation of solitons from an extended pattern. After soliton generation the comb exhibits the sech^2 spectral envelope and quiet repetition-rate tone characteristic of single-soliton operation, shown in Figs. 4(b) and 4(c). Once single-soliton operation is achieved, α may be increased again without loss of the soliton, consistent with the level diagram shown in Fig. 1(b). We have verified that it is possible to turn off the PM while preserving the soliton if the PM is turned off by first decreasing its amplitude slowly (i.e., on the timescale of 1 s) before turning it off entirely (see also Ref. [16]).

To investigate the repeatability of our technique, we automate soliton generation by repeatedly decreasing α from a large initial value and then increasing it again—control of α is achieved through adjustment of f_{PDH}. The termination points of the scan are chosen such that at the lower end of the scan a soliton is generated before α begins to increase again, and at the upper end of the scan the soliton has been lost (because the maximum

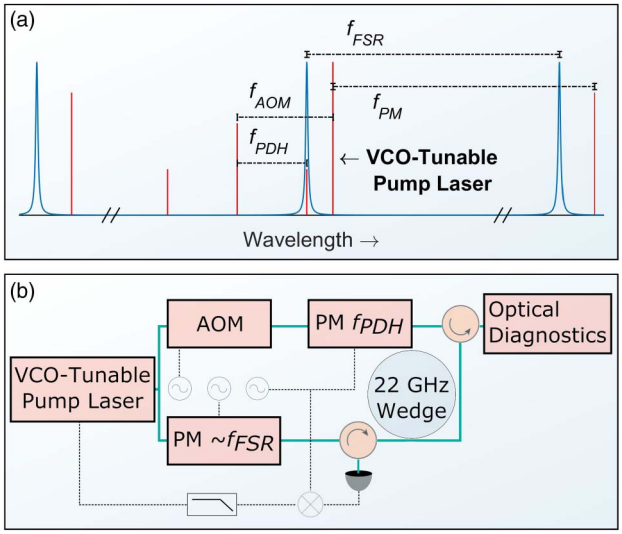

Fig. 3. (a) Frequency-domain depiction of the experiment, with cavity modes shown in blue and laser frequencies shown in red. Modulation of a counter-propagating probe beam at f_{PDH} after shifting by f_{AOM} and subsequent locking of the red PDH sideband to the resonance allows detuning control via $\nu_0 - \nu_{\mathrm{pump}} = f_{\mathrm{AOM}} - f_{\mathrm{PDH}}$, with adjustments implemented by changing f_{PDH}. (b) Schematic depiction of the components of the experiment used for frequency control of the system.

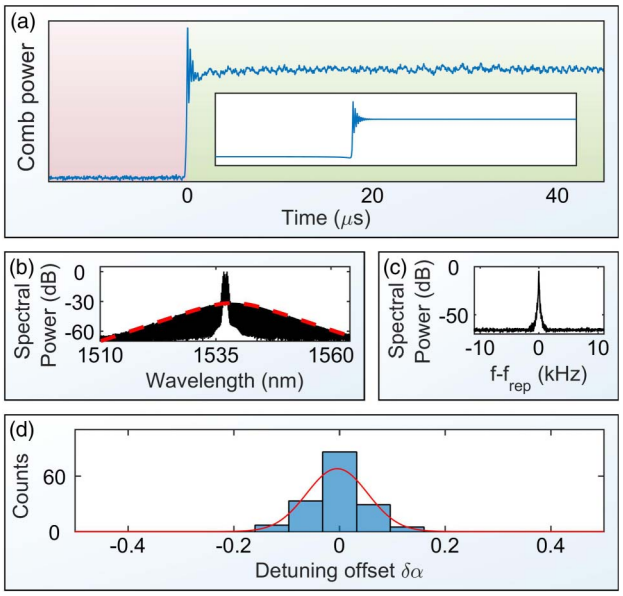

Fig. 4. (a) Measurement of a reversed soliton step in the comb power associated with soliton generation from the background. Inset shows qualitatively similar dynamics observed in an LLE-simulated comb-power trace. (b) Measured optical spectrum of the soliton generated with a phase-modulated pump laser. The spectrum of the pump, which contains phase-modulation sidebands, is visible in the center. The soliton's spectral envelope closely matches the sech^2 envelope that has been overlaid in dashed red. (c) Plot of the out-coupled soliton pulse train's repetition rate as recorded by a photodetector, exhibiting a characteristically high signal-to-noise ratio. We emphasize that this data is obtained with the phase modulation turned off; otherwise the recorded RF signal is dominated by through-coupled phase-modulation sidebands at $f_{\mathrm{PM}} \sim f_{\mathrm{FSR}} \sim f_{\mathrm{rep}}$. (d) Histogram of measured offset in detuning from a reference value at which a soliton is generated over 160 successive trials, with a Gaussian fit shown in red. The width of the interval over which solitons are generated is larger than the calculated width of the protected $N = 1$ level shown in Fig. 1(b), but the model does not include laser fluctuations and other experimental effects.

detuning for soliton existence has been exceeded) before α begins to decrease. Specifically, the scan runs linearly between detuning values of approximately 5 and 20 MHz. We observe generation and extinction of 1000 solitons in 1000 trials over 100 s with this automated scan, with a 100% measured success rate indicated by the comb-power trace recorded during the repeated sweep. Our probe-laser setup enables measurement of the detuning at which soliton generation occurs, which changes little from run to run. Figure 4(d) presents a histogram of detuning measurements for the generation of 160 solitons.

4. EXPERIMENTAL RESULTS: SOLITON CONTROL

Besides enabling protected single-soliton operation, PM pumping also naturally provides timing and repetition-rate control, because the solitons are pushed toward the intracavity phase maximum [15]. We explore this control, with results summarized in Fig. 5. In our experiments, the repetition rate of the out-coupled pulse train (f_{rep}) remains locked to f_{PM} over a bandwidth of $\sim \pm 40$ kHz. In Fig. 5(a), we show a spectrogram of f_{rep} measured as f_{PM} is swept sinusoidally over ± 50 kHz. The repetition rate follows the PM except for glitches near the peaks of the sweep. In the inset of Fig. 5(a) we overlay the results of LLE simulations (see below) that qualitatively match the observed behavior. These simulations indicate that the periodic nature of the glitches is due to the residual pulling of the phase modulation on the soliton when the latter periodically cycles through the pump's phase maximum. Our observed locking range of $\sim \pm 40$ kHz agrees well with an estimate $\delta_{\mathrm{PM}} \times D_2/2\pi \sim 44$ kHz [15] using the approximate measured value $D_2/2\pi = 14$ kHz per mode and modulation depth $\delta_{\mathrm{PM}} = \pi$.

To investigate fast control of the repetition rate, we measure f_{rep} as f_{PM} is rapidly switched by ± 40 kHz around the soliton's natural repetition rate. We plot the resulting data as eye diagrams in Figs. 5(b) and 5(c). In Fig. 5(b), f_{PM} is switched with 200 μs period and 10 μs transition time; in Fig. 5(c) it is switched with 100 μs period and 60 ns transition time. This data is obtained by detecting a portion of the pulse train's spectrum that excludes the pump laser with a sufficiently fast photodetector and passing the resulting f_{rep} signal through two paths, one with an element that induces a frequency-dependent phase shift. After calibration, the repetition rate can be obtained from the resulting phase shift in real time. These eye diagrams show that the PM enables exquisite control of the soliton pulse train.

We perform LLE simulations to further explore the dynamics of repetition-rate switching. We introduce the term $+\beta_1 \frac{\partial \psi}{\partial \theta}$ to the right-hand side of Eq. (1), where $\beta_1 = -2(f_{\mathrm{FSR}} - f_{\mathrm{PM}})/\Delta\nu$ represents a difference between the modulation frequency and the FSR of the resonator near the pump wavelength [15,16]; β_1 may be varied in time. In Fig. 5(c) we overlay a simulation of switching conducted for parameters ($\Delta\nu = 1.5$ MHz, $\delta_{\mathrm{PM}} = 0.9\pi$) near the experimental values, and the agreement between measurements and simulation indicates that the measurements are consistent with fundamental LLE dynamics. We present the results of additional simulations in Fig. 5(d); the basic observation is that the switching speed of f_{rep} is limited by the resonator linewidth, and can be modestly improved by increasing δ_{PM}.

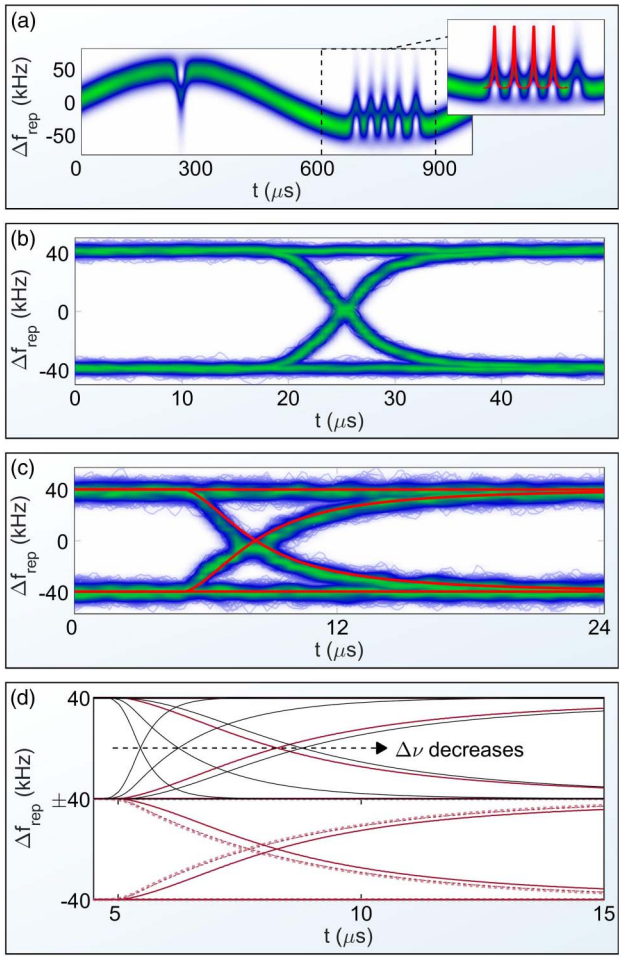

Fig. 5. (a) Measured spectrogram of f_{rep} as f_{PM} is swept over ± 50 kHz, with glitches where the locking range is exceeded. Inset: qualitative agreement with simulations, shown in red, when f_{PM} is outside of the locking bandwidth. As the soliton and the pump phase evolve at different frequencies f_{rep} and f_{PM}, the soliton periodically approaches the maximum of the phase profile. The soliton's group velocity changes, nearly locking to the phase modulation, before becoming clearly unlocked again. (b) Measured eye diagram of f_{rep} as f_{PM} is switched ± 40 kHz with 10 μs transition time. (c) The same with 60 ns transition time, and an LLE simulation of the dynamics (red) with depth $\delta_{\mathrm{PM}} = 0.9\pi$ and resonator linewidth $\Delta\nu = 1.5$ MHz. (d) Simulated switching dynamics for various linewidths and modulation depths. The theory trace from (c) is reproduced in solid red in both panels. Top, solid black: modulation depth 0.9π as in (c), and $\Delta\nu = 10$ MHz (fastest, left), 3 MHz, and 1.4 MHz. Bottom, dashed red: linewidth $\Delta\nu = 1.5$ MHz as in (c), with modulation depths of 2π and 6π (curves nearly overlap).

5. APPLICATION OF THE TECHNIQUE TO HIGH FREE-SPECTRAL RANGE RESONATORS VIA SUBHARMONIC PHASE MODULATION

One apparent barrier to the use of PM for protected single-soliton operation is the electronically inaccessible FSRs of some microcomb resonators. However, this challenge can be overcome by applying PM at a subharmonic of the FSR. Simulations indicate that solitons can be generated with small modulation depth, e.g., $\delta_{\mathrm{PM}} = 0.15\pi$. In this limit only the first-order PM sidebands are relevant, and their amplitude and phase relative to the carrier

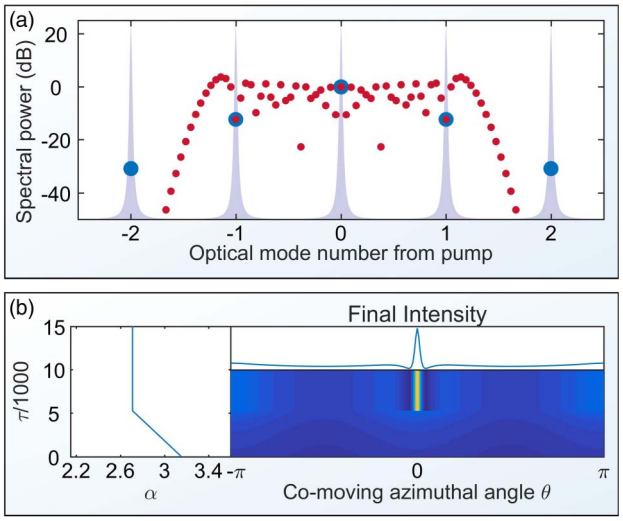

Fig. 6. (a) Simulated spectra of PM at f_{FSR} with depth 0.15π (blue) and at $f_{\mathrm{FSR}}/21$ with depth $\sim 8.3\pi$ (red). The relationships between the fields that address resonator modes −1, 0, and 1 (as indicated by the gray Lorentzian curves) are the same in both cases. (b) LLE simulation of single-soliton generation using the subharmonic phase-modulation spectrum shown in red in panel (a). Only modes $n = 0, \pm 21, \pm 42, \ldots$ of the phase-modulated driving field are coupled into the resonator and affect the LLE dynamics, with modes $|n| > 21$ having negligible power. As α is decreased from a large initial value, a soliton is spontaneously generated, as in the case of phase modulation near the FSR.

control the dynamics. A small desired modulation depth $\delta_{\mathrm{PM,eff}}$ defined by the relationship between the carrier and the lowest order sidebands that are coupled into the resonator can be obtained by modulating with depth δ_{PM} at a frequency $f_{\mathrm{PM}} \sim f_{\mathrm{FSR}}/N$, so that the Nth-order PM sidebands and the carrier address resonator modes with relative mode numbers −1, 0, and 1, where δ_{PM} is chosen in order to achieve effective depth $\delta_{\mathrm{PM,eff}}$. When N is odd, PM is recovered when the sidebands of order $-N$, 0, and N address resonator modes −1, 0, and 1. When N is even, pure AM results, with a driving term like $F(1 + A\cos\theta)$.

Figure 6 presents a simulated example of this technique. In general, the values δ_{PM}, N, and $\delta_{\mathrm{PM,eff}}$ are related non-trivially through Bessel functions according to the Jacobi–Anger expansion (see, e.g., Ref. [27], Section 10.12); for this example we choose $N = 21$ and $\delta_{\mathrm{PM,eff}} = 0.15\pi$. To achieve this effective modulation depth we employ real phase modulation depth of $\delta_{\mathrm{PM}} \sim 8.3\pi$ at $f_{\mathrm{PM}} = f_{\mathrm{rep}}/21$. The phase modulation spreads the optical power into the PM sidebands, so this technique requires higher optical power for the same effective pumping strength; in this example, the power must be increased by ∼15.6 dB. In fact, $\delta_{\mathrm{PM,eff}} = 0.15\pi$ can be recovered with smaller δ_{PM}; however, this comes with far lower spectral efficiency (as defined by the fraction of total optical power that is coupled into the resonator). While the required modulation depth and pump power are higher with subharmonic PM, neither is impractical. This technique could be used for protected single-soliton generation and operation in high-repetition-rate systems; the example above indicates that it could be immediately applied to deterministic single-soliton generation in a 630 GHz FSR resonator with 30 GHz phase modulation. In principle, the ratio $N = f_{\mathrm{FSR}}/f_{\mathrm{PM}}$ can be increased, allowing smaller phase-modulation frequencies to be applied to a given resonator; however, this comes at the cost of lower spectral efficiency and correspondingly higher required total optical power.

6. FINAL REMARKS

In this work, we have shown that phase modulation of the pump laser fundamentally changes a resonator's excitation spectrum and enables an interesting new regime of protected single-soliton operation. In our experiments phase modulation of the pump laser, combined with our approach for detuning control, enabled deterministic, on-demand soliton generation with an observed 100% success rate. While our proof-of-concept experiments made use of sophisticated frequency- and detuning-control techniques, we expect simplification of the approach to be possible in the future, and this will facilitate its implementation in systems for photonics applications.

This technique is applicable to resonators with electronically accessible f_{rep}, which are important components of proposals for photonic integration of Kerr solitons [28,29], and can reach higher repetition-rate systems via subharmonic modulation. After soliton generation, the PM can optionally be turned off, recovering the properties of the non-PM soliton. We expect this technique to enable new experiments. For example, in principle, PM-pumped solitons are generated with known absolute timing, enabling immediate transduction of the modulation phase onto the pulse train; this is impossible with solitons stochastically condensed from an extended pattern. Our work brings microresonator solitons closer to applications.

Funding. National Aeronautics and Space Administration (NASA); National Institute of Standards and Technology (NIST); Defense Advanced Research Projects Agency (DARPA) (DODOS); National Science Foundation (NSF) (DGE 1144083); Air Force Office of Scientific Research (AFOSR) (FA9550-16-1-0016); RSNZ.

Acknowledgment. We thank Su-Peng Yu and Hojoong Jung for comments on the manuscript, and Andrew Weiner for helpful discussions.

REFERENCES

1. T. Herr, V. Brasch, J. D. Jost, C. Y. Wang, N. M. Kondratiev, M. L. Gorodetsky, and T. J. Kippenberg, "Temporal solitons in optical microresonators," Nat. Photonics **8**, 145–152 (2014).
2. X. Yi, Q.-F. Yang, K. Y. Yang, M.-G. Suh, and K. Vahala, "Soliton frequency comb at microwave rates in a high-*Q* silica microresonator," Optica **2**, 1078–1085 (2015).
3. D. C. Cole, E. S. Lamb, P. Del'Haye, S. A. Diddams, and S. B. Papp, "Soliton crystals in Kerr resonators," Nat. Photonics **11**, 671–676 (2017).
4. B. Yao, S. W. Huang, Y. Liu, A. K. Vinod, C. Choi, M. Hoff, Y. Li, M. Yu, Z. Feng, D. L. Kwong, Y. Huang, Y. Rao, X. Duan, and C. W. Wong, "Gate-tunable frequency combs in graphene-nitride microresonators," Nature **558**, 410–414 (2018).
5. X. Xue, Y. Xuan, Y. Liu, P.-H. Wang, S. Chen, J. Wang, D. E. Leaird, M. Qi, and A. M. Weiner, "Mode-locked dark pulse Kerr combs in normal-dispersion microresonators," Nat. Photonics **9**, 594–600 (2015).
6. K. Luo, J. K. Jang, S. Coen, S. G. Murdoch, and M. Erkintalo, "Spontaneous creation and annihilation of temporal cavity solitons in a coherently driven passive fiber resonator," Opt. Lett. **40**, 3735–3738 (2015).
7. C. Joshi, J. K. Jang, K. Luke, X. Ji, S. A. Miller, A. Klenner, Y. Okawachi, M. Lipson, and A. L. Gaeta, "Thermally controlled comb generation and soliton modelocking in microresonators," Opt. Lett. **41**, 2565–2568 (2016).

8. H. Guo, M. Karpov, E. Lucas, A. Kordts, M. H. P. Pfeiffer, V. Brasch, G. Lihachev, V. E. Lobanov, M. L. Gorodetsky, and T. J. Kippenberg, "Universal dynamics and deterministic switching of dissipative Kerr solitons in optical microresonators," Nat. Phys. **13**, 94–102 (2017).
9. X. Yi, Q.-F. Yang, K. Y. Yang, and K. Vahala, "Active capture and stabilization of temporal solitons in microresonators," Opt. Lett. **41**, 2037–2040 (2016).
10. S. B. Papp, P. Del'Haye, and S. A. Diddams, "Parametric seeding of a microresonator optical frequency comb," Opt. Express **21**, 17615–17624 (2013).
11. S. B. Papp, K. Beha, P. Del'Haye, F. Quinlan, H. Lee, K. J. Vahala, and S. A. Diddams, "Microresonator frequency comb optical clock," Optica **1**, 10–14 (2014).
12. V. E. Lobanov, G. V. Lihachev, N. G. Pavlov, A. V. Cherenkov, T. J. Kippenberg, and M. L. Gorodetsky, "Harmonization of chaos into a soliton in Kerr frequency combs," Opt. Express **24**, 27382–27394 (2016).
13. E. Obrzud, S. Lecomte, and T. Herr, "Temporal solitons in microresonators driven by optical pulses," Nat. Photonics **11**, 600–607 (2017).
14. J. K. Jang, M. Erkintalo, S. G. Murdoch, and S. Coen, "Writing and erasing of temporal cavity solitons by direct phase modulation of the cavity driving field," Opt. Lett. **40**, 4755–4758 (2015).
15. J. K. Jang, M. Erkintalo, S. Coen, and S. G. Murdoch, "Temporal tweezing of light through the trapping and manipulation of temporal cavity solitons," Nat. Commun. **6**, 7370 (2015).
16. H. Taheri, A. A. Eftekhar, K. Wiesenfeld, and A. Adibi, "Soliton formation in whispering-gallery-mode resonators via input phase modulation," IEEE Photon. J. **7**, 2200309 (2015).
17. Y. K. Chembo and C. R. Menyuk, "Spatiotemporal Lugiato-Lefever formalism for Kerr-comb generation in whispering-gallery-mode resonators," Phys. Rev. A **87**, 053852 (2013).
18. S. Coen, H. G. Randle, T. Sylvestre, and M. Erkintalo, "Modeling of octave-spanning Kerr frequency combs using a generalized mean-field Lugiato-Lefever model," Opt. Lett. **38**, 37–39 (2013).
19. C. Godey, I. V. Balakireva, A. Coillet, and Y. K. Chembo, "Stability analysis of the spatiotemporal Lugiato-Lefever model for Kerr optical frequency combs in the anomalous and normal dispersion regimes," Phys. Rev. A **89**, 063814 (2014).
20. J. Hult, "A fourth-order Runge-Kutta in the interaction picture method for simulating supercontinuum generation in optical fibers," J. Lightwave Technol. **25**, 3770–3775 (2007).
21. A. M. Heidt, "Efficient adaptive step size method for the simulation of supercontinuum generation in optical fibers," J. Lightwave Technol. **27**, 3984–3991 (2009).
22. S. Coen and M. Erkintalo, "Universal scaling laws of Kerr frequency combs," Opt. Lett. **38**, 1790–1792 (2013).
23. D. C. Cole, K. M. Beha, S. A. Diddams, and S. B. Papp, "Octave-spanning supercontinuum generation via microwave frequency multiplication," J. Phys. Conf. Ser. **723**, 012035 (2016).
24. H. Lee, T. Chen, J. Li, K. Y. Yang, S. Jeon, O. Painter, and K. J. Vahala, "Chemically etched ultrahigh-*Q* wedge-resonator on a silicon chip," Nat. Photonics **6**, 369–373 (2012).
25. J. R. Stone, T. C. Briles, T. E. Drake, D. T. Spencer, D. R. Carlson, S. A. Diddams, and S. B. Papp, "Thermal and nonlinear dissipative-soliton dynamics in Kerr-microresonator frequency combs," Phys. Rev. Lett. **121**, 063902 (2018).
26. T. Carmon, L. Yang, and K. J. Vahala, "Dynamical thermal behavior and thermal self-stability of microcavities," Opt. Express **12**, 4742–4750 (2004).
27. F. W. Olver, D. W. Lozier, R. F. Boisvert, and C. W. Clark, eds., *NIST Handbook of Mathematical Functions* (Cambridge University, 2010).
28. D. T. Spencer, T. Drake, T. C. Briles, J. Stone, L. C. Sinclair, C. Fredrick, Q. Li, D. Westly, B. R. Ilic, A. Bluestone, N. Volet, T. Komljenovic, L. Chang, S. H. Lee, D. Y. Oh, M. Suh, K. Y. Yang, M. H. P. Pfeiffer, T. J. Kippenberg, E. Norberg, L. Theogarajan, K. Vahala, N. R. Newbury, K. Srinivasan, J. E. Bowers, S. A. Diddams, and S. B. Papp, "An optical-frequency synthesizer using integrated photonics," Nature **557**, 81–85 (2018).
29. T. C. Briles, J. R. Stone, T. E. Drake, D. T. Spencer, C. Fredrick, Q. Li, D. Westly, B. R. Ilic, K. Srinivasan, S. A. Diddams, and S. B. Papp, "Interlocking Kerr-microresonator frequency combs for microwave to optical synthesis," Opt. Lett. **43**, 2933–2936 (2018).